Numerical Study of Longitudinal Vein Effects on the Aerodynamic Characteristics of a Corrugated Bio-Airfoil

Shidvash Vakilipour[a,b,*], Hadi Zarafshani[a], Jafar Al Zaili[c]

[a] *Faculty of New Sciences and Technologies, University of Tehran, Tehran, Iran*
[b] *Department of Mechanical Engineering, University of Manitoba, Winnipeg, MB R3T 5V6, Canada*
[c] *Department of Mechanical Engineering and Aeronautics, City, University of London, Northampton Square, London, UK*

Abstract

The purpose of present study is to investigate the influence of cross sectional veins topology on the flow pattern and resulted aerodynamic performance of an oscillating corrugated bio-inspired airfoil. To demonstrate the vein effects, a cross section of the Ashena Cyanea wing is modeled with three configurations. The air flow passing bio-airfoil is subjected to three Reynolds numbers of 1000, 5000, and 14000 and selected reduced frequencies (k) and angular amplitude (A). The results show that as the Reynolds number increases the effects of veins structure become more significant. The lift coefficients of the three studied bio-airfoils, over the range of Reynolds numbers, are close to each other considered in this work. At the Reynolds numbers of 1000 and 5000, the thin bio-airfoil has minimum drag coefficient and the drag coefficients of thick and veined bio-airfoils are quite similar. The veins in the bio-airfoils increase the drag coefficient significantly for the Reynolds numbers of 14000 compared to the Reynolds number of 5000. Finally, the numerical simulations provide hysteresis of lift and drag coefficients subjected to an increment for Reynolds number, reduced frequency, and angular amplitude.

Keywords: Bio-inspired pitching airfoil, OpenFOAM, low Reynolds k-ω

*Corresponding author
Email address: vakilipour@ut.ac.ir (Shidvash Vakilipour)

SST-SAS model, lift and drag coefficients

2010 MSC: 00-01, 99-00

1. INTRODUCTION

The flight of insects, especially dragonflies, has fascinated scientists with particular focus on the investigation of their flight mechanism to design airfoils with better aerodynamic performance [1]. Insects benefit from single or tandem flapping wing configurations with a corrugated airfoil section which are the main origins of their efficient aerodynamic and maneuver performance [2]. Srygley and Thomas [3] performed experiments to investigate the lift generation mechanism of a butterfly during its free-flying maneuver. They observed that it is composed of wake capturing, active and inactive upstrokes, generation of leading-edge vortices, and rotation and “clap and fling” movements. Ellington et al. [4] carried out visualizations of airflow around the wings of a Hawkmoth Manduca Sexta. They found out that the leading-edge vortex formed during the downstroke is one of the main sources of lift forces. The flight of dragonfly is also studied by the researchers who are interested in understand and analyze its mechanism and performance [5, 6, 7, 8, 9, 10]. Dragonflies are equipped with a tandem wing configuration and fly at Reynolds numbers lower than 15000 [10]. They perform in-phase and out-of-phase wing flapping in take-off and forward flight, respectively [5]. In-phase flapping produces high aerodynamic forces, on the other hand, flapping out of phase results in a better flight efficiency [11, 7, 9].

From structural viewpoint, the surface topography and cross-section (bio-airfoils) of insect wings are corrugated with an irregular pattern [12]. Therefore, flow patterns and wake regions around and behind a bio-airfoil are affected by vortices formed within its surface cavities [13]. Barnes and Visbal [14] showed that the flow transition occur at Reynolds numbers lower than 7500. Validation of the aerodynamic performance of corrugated and smooth wings is a challenging task. For this purpose, Levy and Seifert [15] compared aerodynamic forces of a simplified corrugated dragonfly wing section with an Eppler-E61 airfoil at fixed angles of attack. They demonstrated that the aerodynamic performance of the corrugated airfoil is better than the Eppler-E61 airfoil. Vargas and Mittal [16] numerically compared the performance of corrugated airfoil and flat plate at Reynolds numbers from 500 to 10000. Their study showed that the flat plate and corrugated airfoil performed better than the other at Reynolds numbers lower than and above 5000, respectively. Tamai et al. [17] investigated the flow characteristics around corrugated and smooth airfoils at Reynolds number of 34000. Their experiments revealed that the performance of the corrugated airfoil is superior in preventing stall as compared to the smooth one. Meng and Sun [18] studied the aerodynamic forces exerted on airfoil with different corrugation and flat plate during a gliding motion at the Reynolds numbers between 200 and 2400. They showed that the corrugation decreases the lift force.

Two mechanisms are responsible for this effect; one is that the vortex produced at lower surface of the corrugated airfoils creates local low-pressure regions on the lower surface of the wing. The other is that leading-edge-separation layer pushed by the corrugation near the leading edge, therefore suction pressure and lift are reduced. Flint et al. [13] studied the aerodynamic performance of a pitching corrugated airfoil. They showed that the corrugated airfoil produces thrust force at Strouhal numbers above 0.4. At Strouhal numbers lower than 0.4, the smooth airfoil has better aerodynamic performance. At Strouhal numbers above 0.4, however, there is no data for smooth airfoil to compared with corrugated airfoil. Kwok and Mittal [19] investigated experimentally the aerodynamic performance of corrugated and smooth airfoils. They indicated that the lift coefficients of smooth and corrugated airfoils are nearly the same. Kim et al. [20] numerically investigated effect of the dragonfly wing corrugation on gliding performance at Reynolds numbers 150, 1400, and 10000 and angles attack from 0 to 40. Their results showed that the corrugation increased the lift through all the angles of attack. The drag coefficient was not affected by the surface corrugation. In comparison with a smooth wing, the higher lift force of a corrugated wing was confirmed by [21, 22]. Murphy and Hu [23] performed measurements to compare the aerodynamic performance of a corrugated bio-airfoil with a flat plate at Reynolds numbers between 58000 and 125000. They demonstrated that the lift and drag coefficients of the corrugated bio-airfoil are higher than those of flat plate. New et al. [24] experimentally compared the separation control behaviour of corrugated and NACA0010 airfoils at Re=14000. The results showed that the corrugated airfoils have better flow separation control behavior.

Dragonfly wing consist of a membrane and veins, which varies along the wing span [25, 22]. Rees and christopher [26] explored details of the wing veins of a dragonfly. The investigation of structural characteristics of the corrugated and smooth airfoils showed that a corrugated airfoil has superior performance in terms of bending, deflection, and stress on the wing [25, 27]. Harbig et al. [28] numerically investigated the effect of wing camber on the flow structures and aerodynamic force for insect-like wings. They indicated that the positively cambered improves the aerodynamic performance of a flapping and rotating wing at the Reynolds numbers lower than 1500. Harbig et al. [29] carried out numerical experiments to study the effect of wing aspect ratio (AR) and Reynolds number on the flow structures over a bio-inspired wing. Their simulations showed that an increment in the Reynolds number at an AR of 2.91 increases the lift coefficient. Also, increasing the AR at Reynolds numbers from 120 to 1500 have the same effects on the flow structures and results in an increase in the lift coefficient. Au et al. [30] numerically investigated the effect of the corrugation on the aerodynamic performance of three dimensional camber wings at Reynolds number of 18000. They demonstrated that the suggested corrugated wings have lower aerodynamic forces and performance as compared to non-corrugated wing. Kesel and Antonia [22] performed experiments to measure aerodynamic forces of dragonfly wings with different cross sections at Reynolds numbers of 7880 to 10000. Their Results indicated that the orientation of the leading-edge has no important role on the aerodynamic performance. Okamoto et al. [21] investigated experimentally the effect of thickness, camber, and sharpness of the leading edge on the aerodynamic performance at Reynolds numbers from

Table 1: Geometrical dimensions of the bio-airfoil parameters illustrated in Fig. 1

	t_1(mm)	t_2(mm)	τ_1	τ_2	c(mm)	h(mm)
Thin	0.02	-	4.53	-	81	-
Thick	-	0.762	-	5.49	81	-
Veined	0.02	-	-	5.49	81	0.96

11000 to 15000. They showed that the airfoil with sharper leading edge, more cambered profile and thinner, has better aerodynamic performance.

The present study is organized to investigate the effects of cross sectional veins topology on the flow pattern and aerodynamic performance of an pitching corrugated bio-airfoil. To demonstrate the vein effects, an airfoil section of Ashena Cyanea wing is modeled by veined an un-veined. The Reynolds number of the air flow passing bio-airfoil is set to 1000, 5000, and 14000 to study the effects of vein topology in laminar and turbulent flows. The pitching reduced frequency and amplitude are varied to expose probable vein effects in different flight conditions.

2. BIO-AIRFOILS MODELS

Investigation of aerodynamic influences of longitudinal veins and bio-airfoil thickness is carried out by three computational models of a rigid bio-inspired corrugated airfoil. Figure 1 shows the corrugated bio-airfoil models inspired by the Ashena Cyanea forewing at middle cross section [22]. The veined bio-airfoil is the thin one with veins, and the thick bio-airfoil has the vein thickness. The longitudinal dimension of veins is described by [26]. The geometrical parameters of the bio-airfoils used are given in Table 2.

Figure 2 illustrates the layout of domain and generated grid near and far from the bio-airfoils. Flow domain consists of two sub-domains; outer (stationary) and inner (pitching) domain separated by a sliding surface. The grid within in viscous flow boundary layer is generated by quadrilaterals. The grid resolution adjacent to the walls is adjusted to keep y^+ less than unity for the near wall

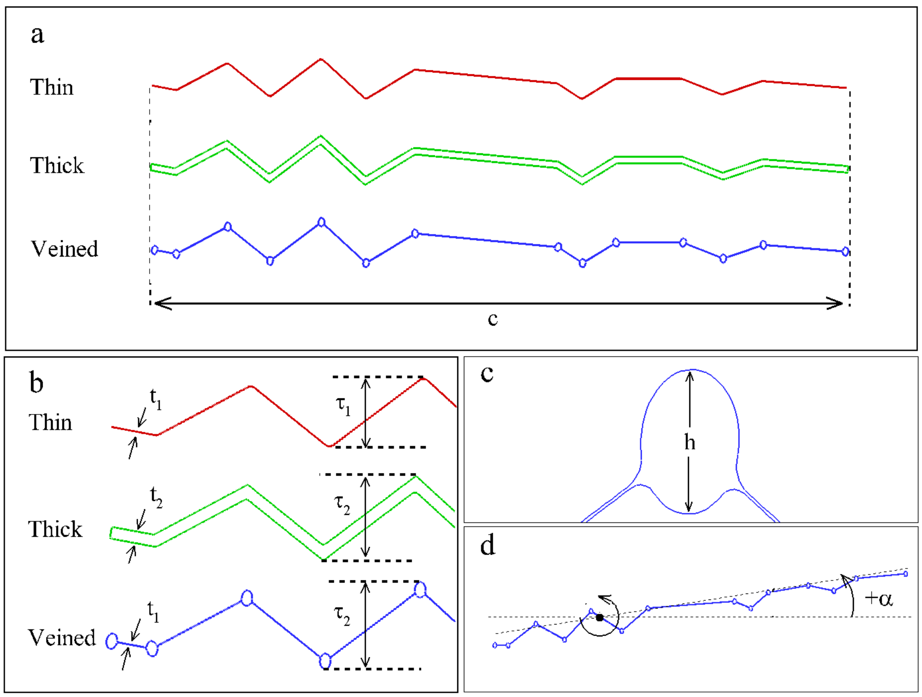

Figure 1: The configuration and nomenclature of modeled bio-airfoils, (a) the overall geometry of the bio-airfoils, (b) the details of the bio-airfoil sections, (c) the dimension parameter of the vein section, and (d) the pitching direction of the bio-airfoil

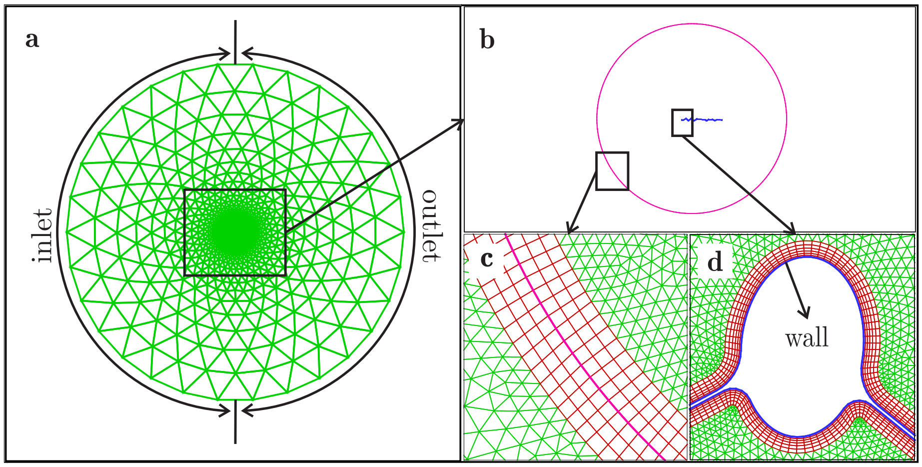

Figure 2: The computational domain and the grid around the bio-airfoils: (a) the flow domain, (b) the sliding surface, (c) the quadrilateral cells near the sliding surface, and (d) the boundary layer quadrilateral cells near the bio-airfoil surface

calculations in turbulence flow modeling.

3. THE NUMERICAL MODELING

The flow field around the pitching corrugated airfoil is modeled by the unsteady incompressible form of continuity and Navier-Stokes flow equations. These equations are written by primitive variables as follows:

$$\nabla.\overrightarrow{V} = 0 \tag{1}$$

$$\frac{\partial\overrightarrow{V}}{\partial t} + (\overrightarrow{V}.\nabla)\overrightarrow{V} = -\frac{\nabla p}{\rho} + \upsilon\,\nabla^2\,\overrightarrow{V} \tag{2}$$

where $\overrightarrow{V}$(u,v,w), p, ρ, and ν are the flow velocity, pressure, density, and fluid kinematic viscosity, respectively.

In this study, the two dimensional flow field around bio-inspired corrugated airfoils are modeled using the Open Source Field Operation and Manipulation Software, OpenFOAM. OpenFOAM provides an open source collection of numerical solvers and utilities for flow and heat transfer. The pitching process of corrugated airfoils are modeled by the sliding mesh technique provided in OpenFOAM using Arbitrary Mesh Interface (AMI).

The implemented boundary condition at the inlet boundary of domain are *fixed value* for velocity and *zeroGradient* for pressure fields. The *zeroGradient* condition for velocity and *fiexed value* pressure are applied at the outlet boundary of domain. The no-slip velocity and zeroGradient condition for the pressure are imposed at the bio-airfoil surface. The *cyclicAMI* condition is implemented for sliding surface between inner and outer domain. The *cyclicAMI* is Coupling condition between a pair of patches that share the same outer bounds, but whose inner construction may be dissimilar. The *pimpleDyMFoam* solver was used to perform computations for the current unsteady moving boundary flow problem. The first order and second order discretization scheme are used to discretize the time and space derivatives, respectively.

In general, the surface topography of insect wings and their sections (bio-airfoils) are corrugated and irregular. In this regard, the flow transition occurs at Reynolds number lower than 7500 [14]. It is indispensable to use appropriate turbulence models to resolve large turbulent structures in time. Therefore, the flow at Reynolds numbers of 1000, 5000, and 14000 are numerically simulated to study the aerodynamic characteristics of bio-airfoils in laminar and turbulent flow regions. Non-linear eddy viscosity turbulence models (NLEVM) superior predict the shedding of the dynamic-stall vortex around pitching airfoil [31, 32]. The $k-\omega$ SST facilitated by Scale-Adaptive Simulation (SAS) turbulence modeling has been used as a pioneer model to carry out separated flow calculations near the corrugated airfoil surface in present study. The $k-\omega$ SST-SAS handles unsteady flow structures well and is the highest fidelity turbulence model available in a two-dimensional simulation. The SAS method uses a RANS based model in regions of steady flow transitioning to an Large-Eddy Simulation (LES) model through multiple stage of turbulent eddy resolution in regions of unsteady flows. It behaves like LES in unsteady solutions but with lower demand for local grid spacing. The concept behind this model is based on the introduction of the von Karman length-scale into the turbulence scale equation. This information allows the SAS model to dynamically adjust to resolved structures in a URANS simulation. This results in a LES-like behavior in unsteady regions and standard RANS behavior in stable regions, which significantly reduces computational expenses and demand for grid spacing required to get a LES-like accuracy in the simulations [33, 34].

The aerodynamic coefficients of pitching bio-airfoils are calculated at reduced frequencies (k) between 1.24, 2.48, and 4.96, and angular amplitude (A) between $A = 2.5°$, $A = 5°$, and $A = 10°$. It is worth mentioning that the pitching axis is at the quarter-chord of the bio-airfoils. The Reynolds number and reduced frequency (k) are defined as:

$$Re = \frac{Uc}{\upsilon} \tag{3}$$

$$k = \frac{\pi f c}{U} \tag{4}$$

where U, c, and f are the free stream velocity, airfoil chord length, and frequency of oscillation, respectively.

In an iterative numerical algorithm, the Courant number (C) threshold is essentially enforced by the relative propagation of the physical and numerical solution information. The Courant number in a computational cell is defined as:

$$C = \frac{U\Delta t}{\Delta h} \tag{5}$$

where Δt is the simulation time-step and Δh is the minimum height (characteristic length) of the grid cells. In present study, all simulations have been carried out by a Courant number below than one.

Pitch angle, α, is calculated from follow equation:

$$\alpha = Asin(2\pi f t) \tag{6}$$

where A, and t are angular amplitude and time, respectively. The lift and drag coefficients, C_L and C_D, are computed using the following formulas:

$$C_L = \frac{f_y}{\frac{1}{2}\rho U^2 c} \tag{7}$$

$$C_D = \frac{f_x}{\frac{1}{2}\rho U^2 c} \quad (8)$$

where f_x and f_y are the fluid flow force along x and y coordinates. Pressure Coefficient, C_p, is calculated from follow equation:

$$C_p = \frac{p - p_\infty}{\frac{1}{2}\rho U^2} \quad (9)$$

where p and p_∞ are pressures at the point of interest and the far field, respectively. The friction Coefficient, C_f, is calculated from the following equation:

$$C_f = \frac{\tau_w}{\frac{1}{2}\rho U^2} \quad (10)$$

where τ_w is the wall shear stress.

4. RESULTS AND DISCUSSION

In order to validate the numerical experiments of the current study, a geometry of bio-airfoil was created and the obtained results have been validated against those of Flint et al. [13]. They had performed a set of experimental tests to validate their numerical modeling qualitatively. Here, the results of the current study have been compared to their numerical simulation results. Figure 3 shows the lift and drag coefficients predicted for the flow around pitching bio-airfoil with $k = 2.48$, $A = 20°$. The comparison between lift and drag coefficients presented in Fig. 3 shows that the present numerical results are in excellent agreement with those of Flint et al. [13].

4.1. The Grid Independence of Solution

In order to investigate the effects of mesh resolution on the numerical results, the flow computations are performed on three meshes with about 115k, 230k, and 350k cells around veined bio-airfoil. A case has been identified to examine the grid independence, where the Reynolds number, reduced frequency and pitching amplitude are $Re = 14000$, $k = 4.96$, $A = 10°$, respectively. A high Reynolds number case has been chosen to ensure that the resolution of the grid

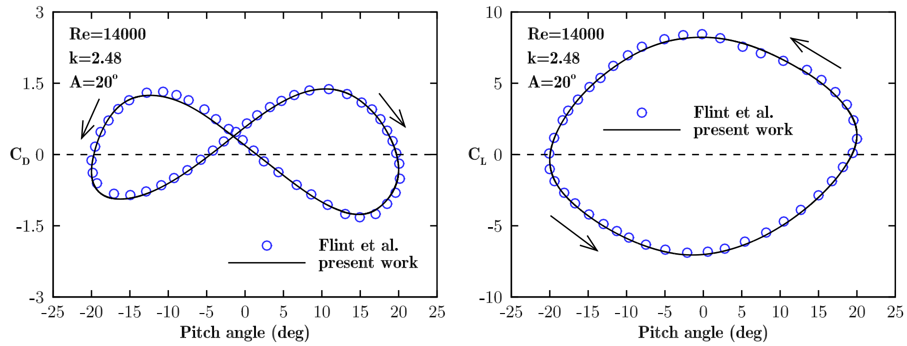

Figure 3: Comparison of lift and drag coefficients calculated from the present flow simulations with the validated results reported by [13] at $k = 2.48$, $A = 20°$

is sufficient to resolve the turbulence effects within the air flow field. Figure 4 demonstrates calculated lift coefficient, C_L, and drag coefficient, C_D, during a period of pitching cycle on three grid resolutions. The numerical results unsurprisingly indicate that the grid with 115k cells has lower accuracy compared to grids with 230k and 350k cells. On the other hand, the numerical results carried out from the flow computations on grids with 230k and 350k cells are acceptably close to each other. As it is seen, the difference between the force coefficients estimated on 350k and 230k grids is significantly lower than those between 115k and 230k.

The maximum difference in the pressure distribution around the bio-airfoil has been adopted as an indicator for the accuracy of the simulations. The maximum difference was observed at higher angles, and higher frequencies. Thus, the grid dependence study has been performed for a case with the highest of these parameters. The maximum difference in the pressure coefficients has been calculated using (L_∞) norm as defined below:

$$L_\infty = max(|{C_{p,i}}^{G1} - {C_{p,i}}^{G2}|, |{C_{p,i}}^{G3} - {C_{p,i}}^{G2}|) \tag{11}$$

Where, ${C_{p,i}}^{G1}$ is the pressure coefficient at point i on the bio-airfoil for the simulation using grid 1 (350k cells). ${C_{p,i}}^{G2}$ and ${C_{p,i}}^{G3}$ are indicating the simulations using 230k and 115k grids, respectively. Figure 5 shows the upper

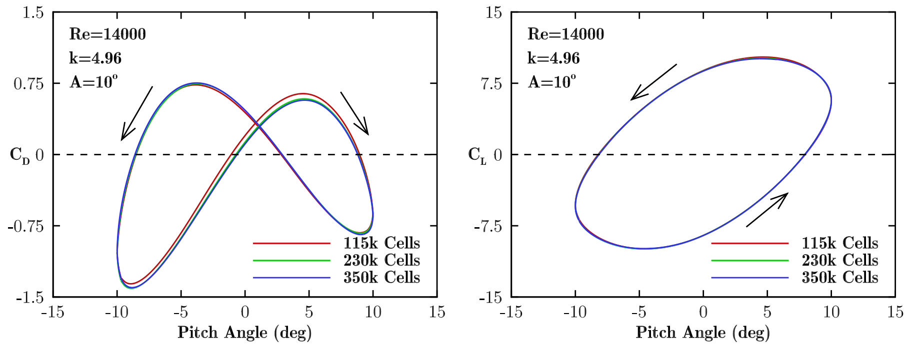

Figure 4: The drag (left) and lift (right) coefficients of the veined bio-airfoil calculated on grids with three resolutions at $k = 4.96$ and $A = 10°$.

and lower surface distribution of pressure coefficient in pitch angle of 10° and −10°. The pressure distribution of the case shown in Figure 5 has a maximum discrepancy at x/c=0.206. The relative (L_∞) norm for pressure distribution of Figure 5 has a reduction factor of 1.8 when comparing the difference in the solutions for 115k and 230k with the one for 230k and 350k.

To quantify the uncertainty of the simulations, a grid convergence index (GCI) has been evaluated. GCI, as suggested by Roache [35], provides an error band for the CFD simulations and it can be an indicator to justify the resolution of the grid in a particular problem. The maximum lift coefficient ($C_{L_{max}}$) within a cycle has been used to study the convergence of the simulations on different grids. The convergence study has been carried out for the veined bio-airfoil. The values of the $C_{L_{max}}$ for $G1$, $G2$ and $G3$ grids are 10.11, 10.17 and 10.29, respectively. The GCI is estimated at 4.93% for $G2$, which is an indicator for the uncertainty of the simulation when using $G2$ grid. The uncertainty is a combination of factors such as grid stretching, grid quality, non-linearities in the solution and turbulence modeling. The detailed calculation of the GCI is provided in Appendix A. Thus, the mesh with 230k cells is employed to simulate air flow around pitching bio-airfoils throughout the present study.

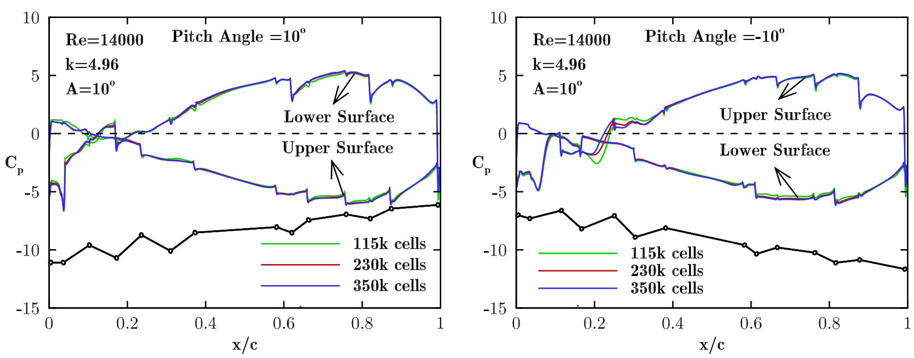

Figure 5: The pressure coefficient on the veined bio-airfoil surface calculated on three grid resolutions at pitch angles of $-10°$ (left) and $10°$ (right)

4.2. The Effects of Angular Amplitude

In this section, the effects of angular amplitude on the aerodynamic coefficients of pitching bio-airfoils are investigated. The dynamic hysteresis of lift and drag coefficients calculated at different angular amplitude and Reynolds numbers are shown in Figs 6-8.

As shown in Fig. 6, the lift coefficients are approximately the same at Re=1000 and A= $10°$. This has also been obtained for A= $2.5°$ and $5°$. The thin bio-airfoil has minimum drag coefficient. The drag coefficient of thick and veined bio-airfoils are close to each other. As is observed, as the angular amplitude increases, there is an ability for producing propulsive force. As shown in Fig. 7, the thin bio-airfoil has the least drag coefficient at Re=5000 such as Re=1000. On the other hand, the bio-airfoil lift coefficients are the same at Re=5000. At Reynolds number of 14000, as shown in Fig. 8, the lift an drag coefficients of bio-airfoils are different. The veined and thin bio-airfoils produce maximum and minimum drag forces, respectively. Fig. 8 shows that as the angular amplitude increases, the difference between the bio-airfoil lift coefficients is reduced.

The total drag force exerted on the flapping bio-airfoils is a result of pressure and friction forces. To assess the pressure and friction forces acting on the pitching bio-airfoils, the dynamic hysteresis pressure and friction drag coef-

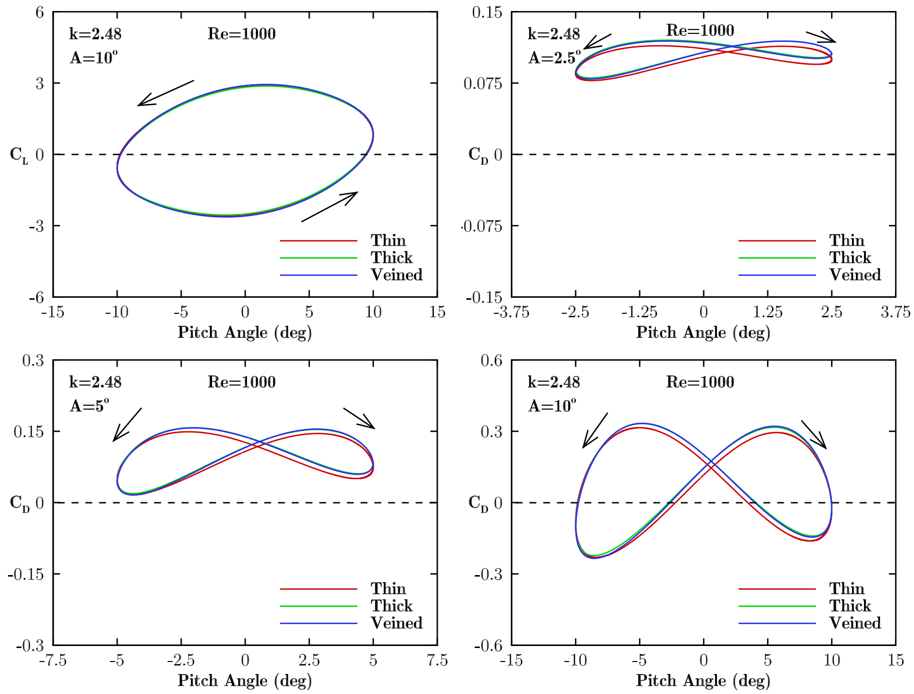

Figure 6: The lift and drag coefficients of bio-airfoils calculated at Re=1000, k= 2.48, and different angular amplitudes

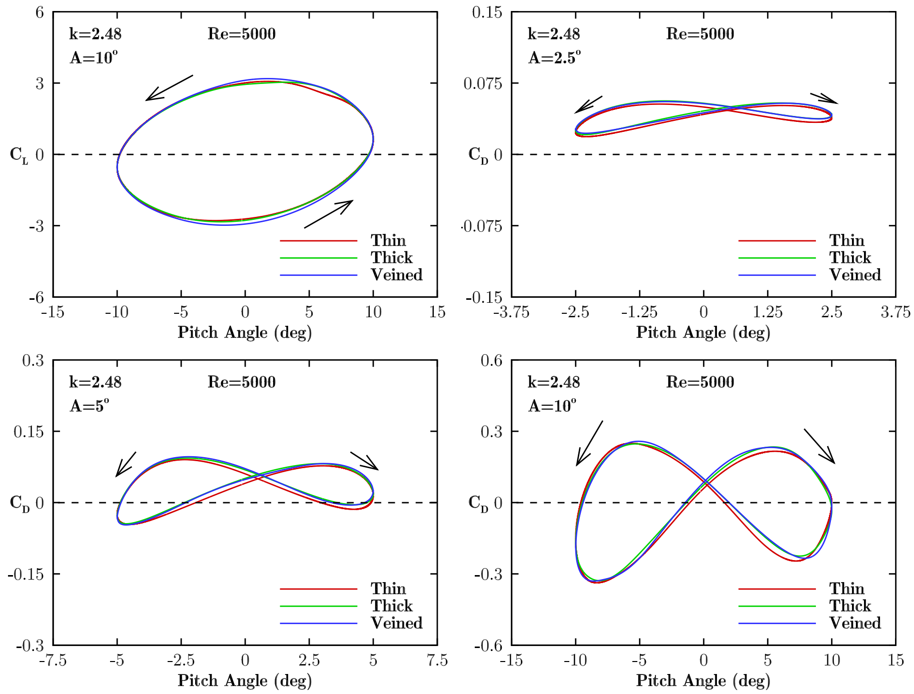

Figure 7: The variation of lift and drag coefficients with pitch angle at Re=5000, k=2.48, and different angular amplitudes

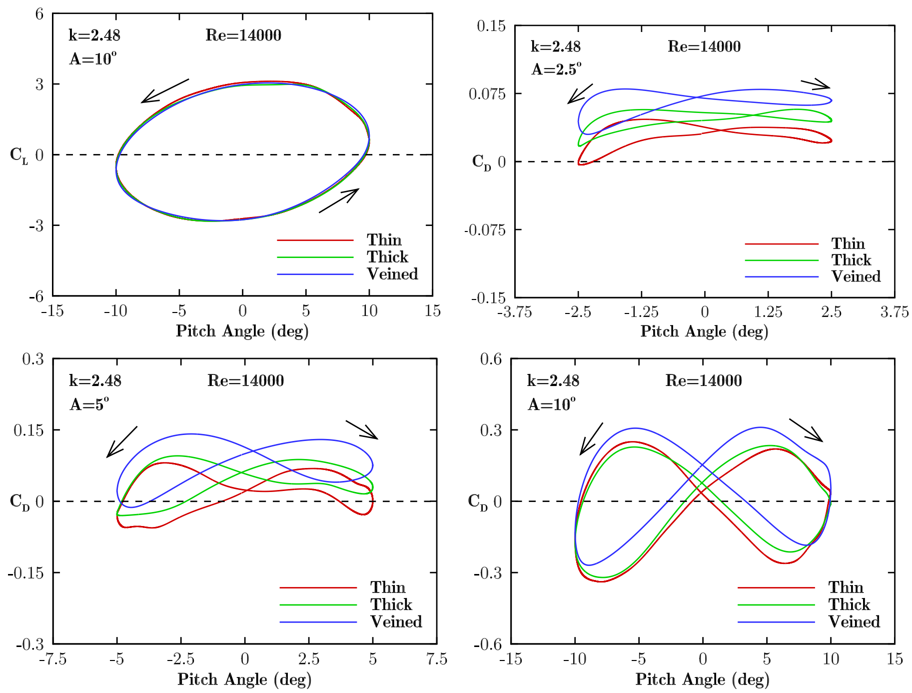

Figure 8: The lift and drag coefficients of bio-airfoils calculated at Re=14000, k=2.48, and different angular amplitudes

ficients of bio-airfoils calculated at $k = 2.48$, $A = 10°$, and Reynolds numbers of 1000, 5000, and 14000 are shown in Fig. 9. The veined bio-airfoil shows maximum pressure drag coefficient, and minimum friction drag coefficient. The pressure and friction drag coefficients of the thin bio-airfoil are minimum and maximum, respectively. The friction drag coefficient decreases as the Reynolds numbers increases from 1000 to 14000 at a fixed reduced frequency and angular amplitude. On the other hand, pressure drag coefficient of bio-airfoil decreases with an increment in Reynolds numbers from 1000 to 5000 and increases with as the Reynolds number reaches to 14000. The numerical results show that the drag force is mostly exerted through the pressure forces in turbulent flow, i.e. $Re = 14000$. On the other hand, both the friction and pressure forces play an important role in producing drag force in laminar flow regime, i.e. $Re = 1000$.

Figure 10 illustrates the pressure coefficient distribution along the bio-airfoil at pitch-down (clockwise rotation) and pitch-up situations. The pressure distribution along airfoil surfaces are approximately the same at laminar flow ($Re = 1000$) and different at turbulent flow ($Re = 14000$) regimes.

Figure 11 shows the flow pattern around three modeled bio-airfoils at selected pitch angles of -2.5, 0, and 2.5 degrees and the Reynolds numbers of 1000 (left) and 14000 (right). At the pitch angle of zero, the flow pattern are illustrated for the pitch up and pitch down situations. The flow pattern are demonstrated using resolved streamlines on a background colored by the pressure contours. At Reynolds number of 1000 (laminar flow), the pressure field and vortices formed around the modeled bio-airfoils are similar. In other words, the vein structures and bio-airfoil thickness do not significantly influence the pressure and velocity fields around the bio-airfoils. The hysteresis loops plotted for lift and drag coefficients at $Re = 1000$ are verified by the the flow patterns in this Figure (see Figs 6 and 9). On the other hand, there are significant differences between the resolved pressure fields and vortices around modeled bio-airfoils at fully turbulent flow regime, i.e. Reynolds number of 14000.

Figure 12 shows the flow pattern in the corrugation (left) and around the leading-edge (right) of three modeled bio-airfoils at selected pitch angle of -2.5

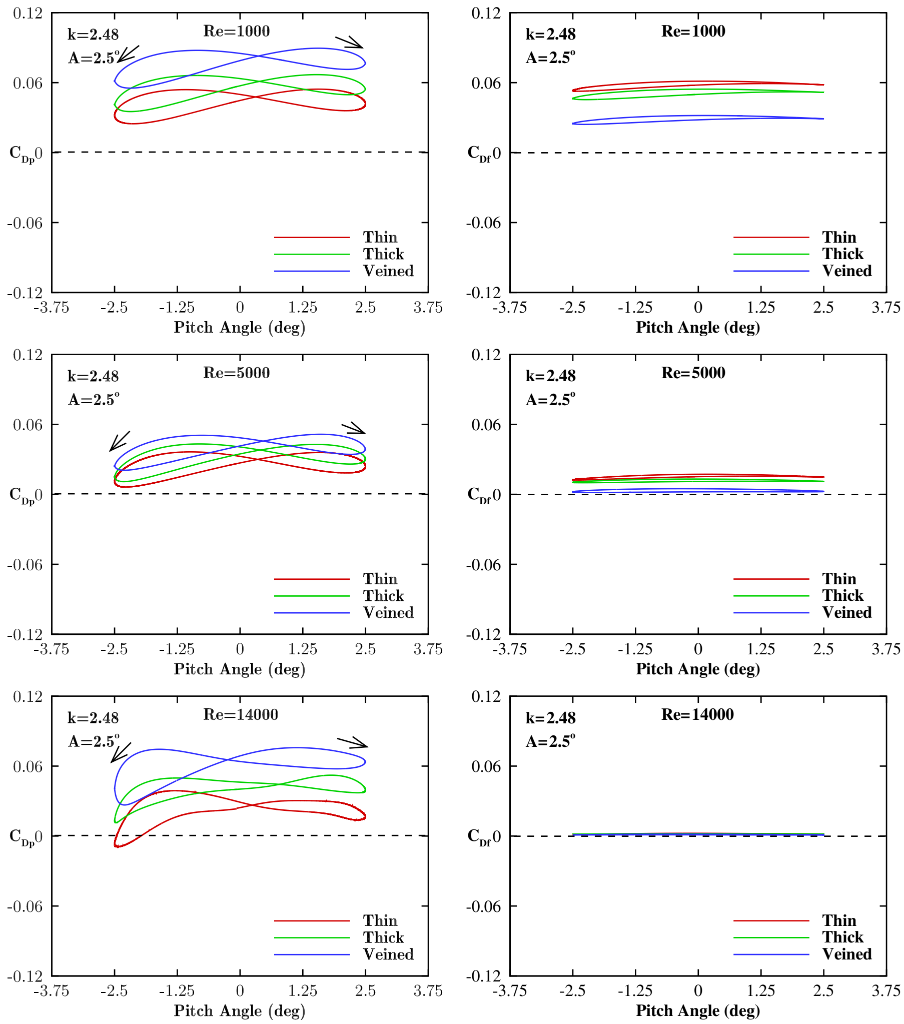

Figure 9: The pressure and friction drag coefficients at k=2.48, $A = 2.5°$, and three Reynolds numbers

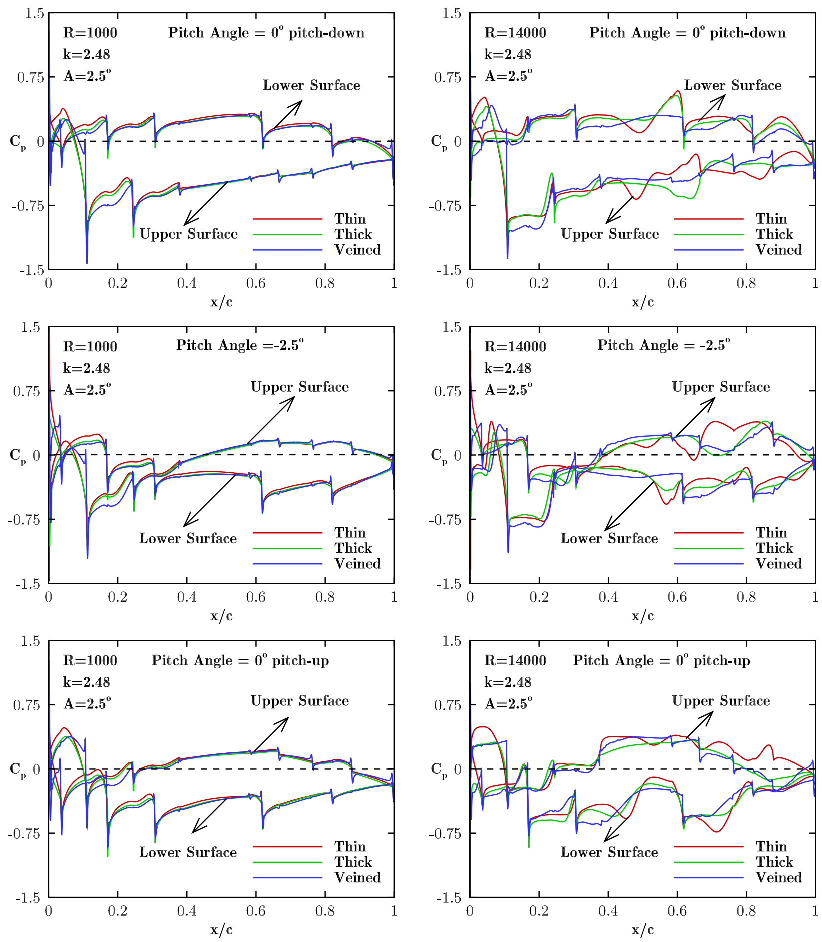

Figure 10: Surface pressure coefficient of bio-airfoils calculated at k=2.48, A=2.5°, and different Reynolds numbers

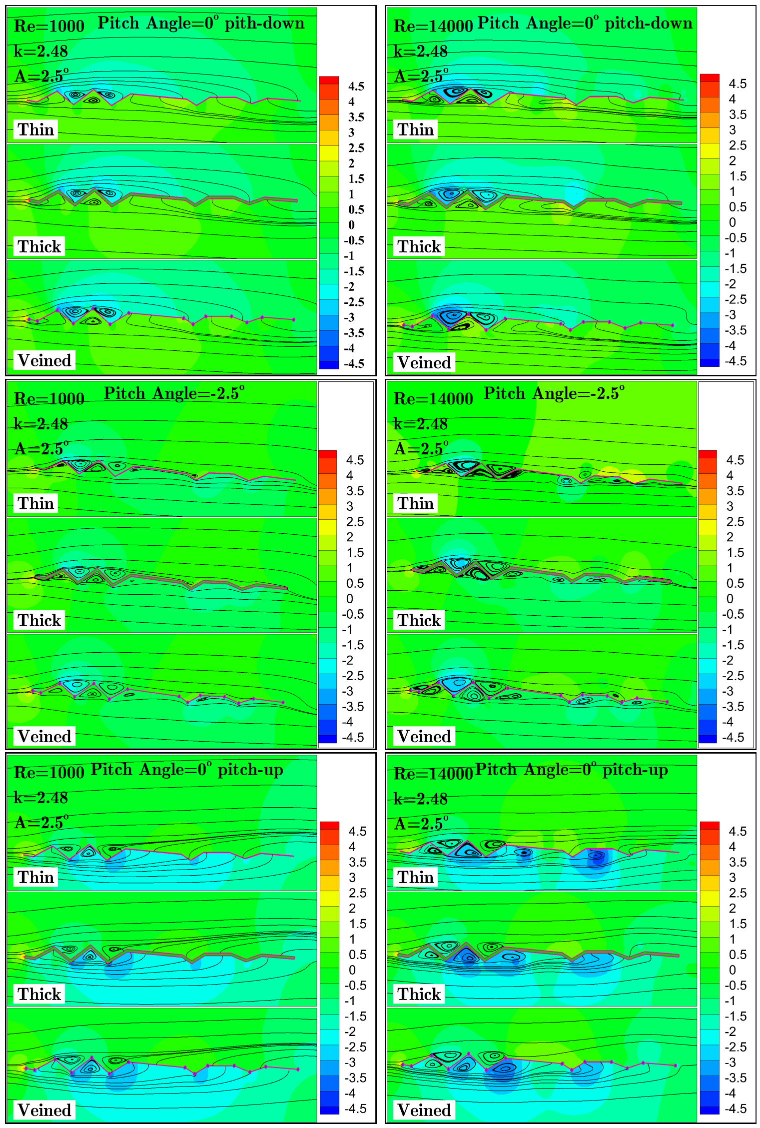

Figure 11: The streamlines and pressure contour within airflow around bio-airfoils calculated at k=2.48, A=2.5° and different Reynolds numbers and pitch angles

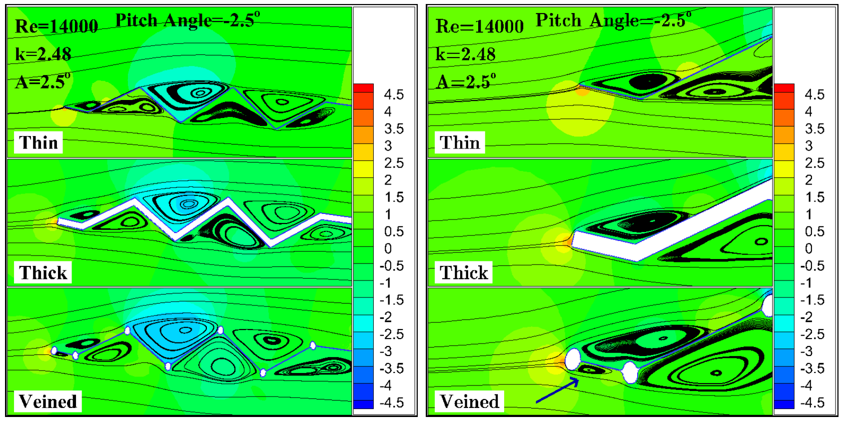

Figure 12: The streamlines and pressure contour within airflow: (Left)in the corrugations; (Right) around leading-edge of bio-airfoils calculated at k=2.48, A=2.5°, and Re=14000

degrees and the Reynolds numbers of 14000. The flow pattern is different in the corrugations of the three different bio-airfoils. Sooraj et al. [36] demonstrated that vortices separation and merging in the corrugation affect pressure variation around the airfoil. Furthermore, the formed vortex below the leading-edge of the veined bio-airfoil, as pointed to in Fig. 12, decreases the suction pressure. Therefore, the pressure difference between upper and lower surfaces of the veined bio-airfoil is lower than those for thin and thick. This demonstrates that as the upstream velocity (flight speed) increases the flow structures around the veined bio-airfoils exerts lower pressure force than those of thin and thick ones. Furthermore, as the Reynolds number increases the vein structures do not increase the friction drag with respect to the two other modeled bio-airfoils (see Fig. 9)

4.3. The Effects of Reduced Frequency

The modeled pitching bio-airfoils are subjected to different oscillation frequencies. In this section, the effects of reduced frequency on the aerodynamic performance of pitching airfoils are investigated. The dynamic hysteresis of the lift and drag coefficients calculated at selected reduced frequencies and Reynolds numbers of 1000, 5000, and 14000 are demonstrated in Figs 13 to 15, respectively. There are three fundamental mechanism that govern aerodynamic efforts acting on the pitching airfoil and which are: leading-edge vortex (force F_{vortex}), added mass reaction (force F_{am}) and leading edge vortex convection and interaction with the wing (wake capture force F_{wc}) [37]:

$$F = F_{vortex} + F_{am} + F_{wc} \tag{12}$$

The Strouhal number (St_c) defined as:

$$St_c = \frac{fc}{U_0} \tag{13}$$

For $St_c < 0.1$, leading edge vortex force becomes dominant; for $0.1 < St_c < 0.5$, added mass force competes with the wake capture force; for $St_c > 0.5$, added mass force becomes dominant. In the present study the reduced frequencies of 1.24, 2.48, and 4.96 have been used. The proportional Strouhal number (St_c) of these reduced frequencies are 0.39, 0.79, and 1.58, respectively. Therefore the effect of added mass reaction is dominant at reduced frequencies of 2.48 and 4.96, while for the lower St_c, added mass and the wake capture lift generation mechanisms are comparable. Added mass is a result of force applied by an accelerating wing on the fluid in its vicinity. Andro and Laurent [37] defined this reaction force as:

$$F_{am} = -\rho \vartheta_{fluid} a \tag{14}$$

Where ϑ is the volume of the fluid displaced by the wing oscillation and a is the acceleration of airfoil. In our case $a(t) = -A\omega^2 sin(\omega t) e_z$, therefore the added mass force is:

$$F_{am} = -\rho \vartheta_{fluid} A\omega^2 sin(\omega t) e_z \tag{15}$$

The force due to added mass reaction is proportional to ω^2, therefore it increment by increasing of reduced frequency.

In Fig. 13, the lift coefficient of three modeled bio-airfoils is approximated with the same values at reduced frequency of k=4.96 and Re=1000. The calculated lift coefficients are following the same trends for k=1.24 and 2.48 at laminar

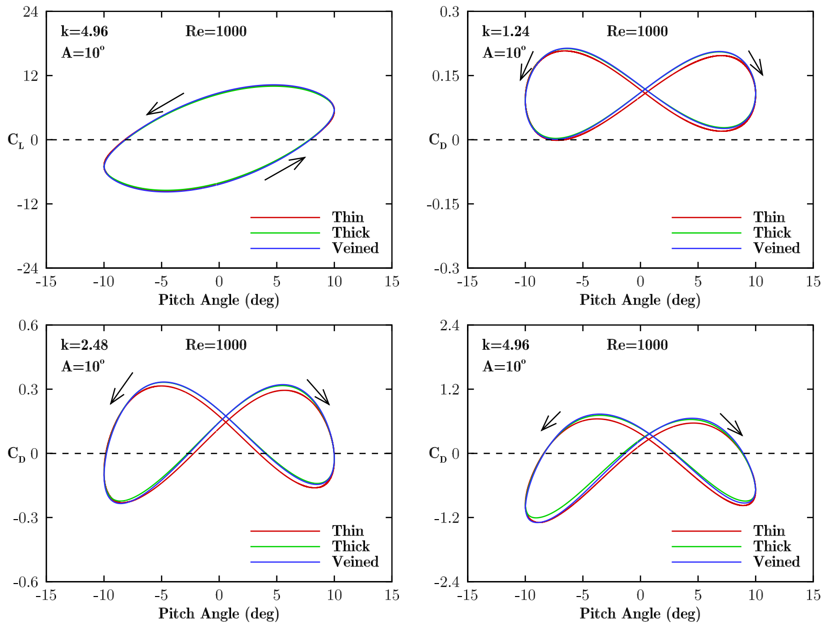

Figure 13: Hysteresis of lift and drag coefficients calculated at Re=1000, A=10°, and selected reduced frequencies

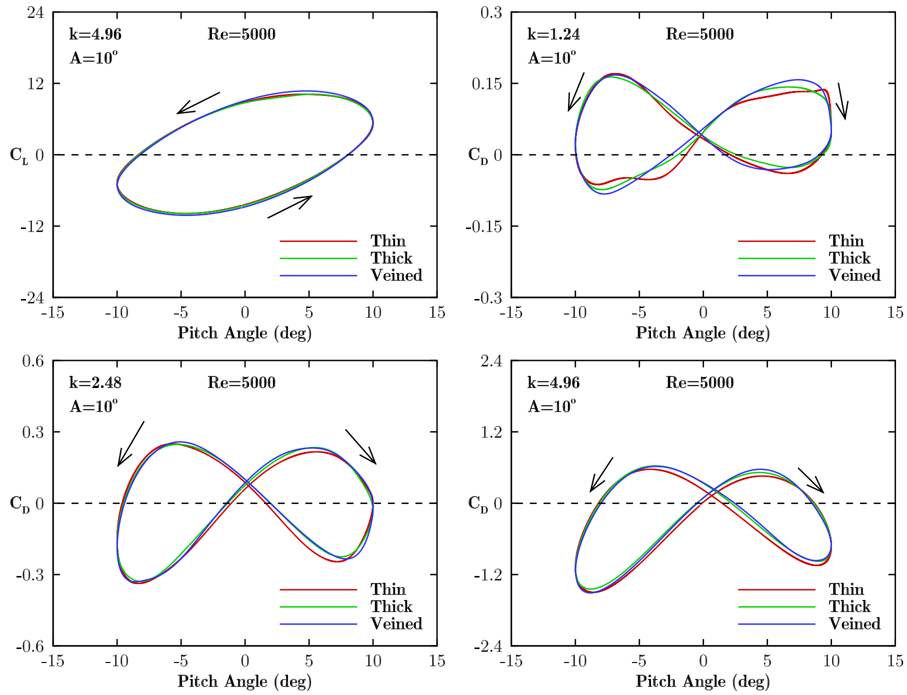

Figure 14: Hysteresis of lift and drag coefficients calculated at Re=5000, A=10°, and selected reduced frequencies

flow regime (Re=1000). On the other hand, the thin bio-airfoil has minimum drag coefficient and the drag coefficient of thick and veined bio-airfoils are predicted close to each other. As is observed, as the reduced frequency increases, there is a possibility for producing propulsive (negative drag) force.

At Re=5000 (Fig. 14), the lift coefficient are similarly obtained for thin, thick, and veined airfoils. With respect to Re=1000, there are more differences between drag coefficients of modeled airfoils at Re=5000. The numerical simulations demonstrate that the aerodynamic loads exerted on the veined airfoil are almost the same as one calculated for the thin and thick ones.

At the Reynolds number of 14000, the lift coefficient is not altered by shape of bio-airfoils at different reduced frequencies. However, the drag coefficient of bio-airfoils are much more different at selected reduced frequencies (see Fig. 15). In this regard, as the reduce frequency decreased, the difference between drag

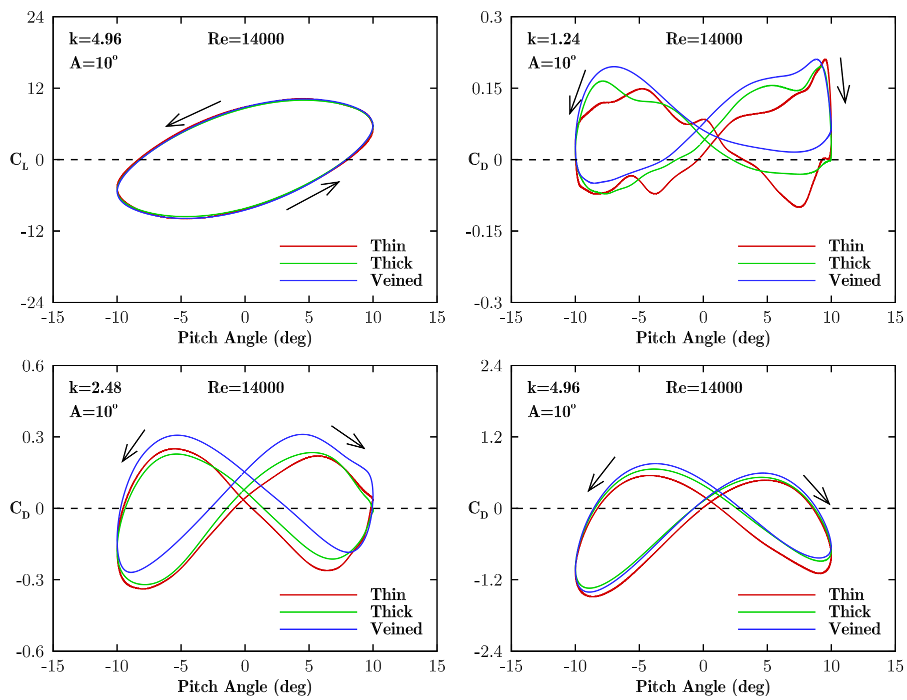

Figure 15: Hysteresis of lift and drag coefficients calculated at Re=14000, A=10°, and selected reduced frequencies

coefficient increases. Moreover, the lowest and highest drag forces are calculated for thin and veined bio-airfoil models, respectively.

4.4. Parametric Study of Veined Bio-Airfoil

In this section, the effects of reduced frequency, angular amplitude, and Reynolds number on the lift and drag coefficient of pitching veined bio-airfoil at different Reynolds numbers have been investigated. Flint et al. [13] showed that the formation and shedding vortices formed inside the bio-airfoil have the most effect on the drag and lift coefficients.

Figure 16 demonstrates the effect of reduced frequency on the dynamic hysteresis in lift and drag coefficients of veined airfoil estimated at A=10° and different Reynolds numbers. As in expected, increasing the reduced frequency results increment in absolute value of C_L, and C_D at most fixed pitch angles and Reynolds numbers.

Figure 17 shows the effect of angular amplitude on the dynamic hysteresis in lift and drag coefficients of veined bio-airfoil estimated at k=2.48 and different Reynolds numbers. At a fixed reduced frequency and Reynolds number, increasing oscillation amplitude results increment in absolute value of C_L, and C_D.

The main outcome revealed from the C_D plots is the effects of change of pitching amplitude and reduced frequency on the propulsion performance of pitching veined bio-airfoil. As is observed from the results, as the angular amplitude or reduced frequency increases, there is an ability for producing propulsive force.

Figure 18 demonstrates the variation of the $C_{L_{max}}$ (maximum instantaneous lift coefficient within a cycle) with angular amplitude and reduced frequency. The results show that as the reduced frequency increases the variation of the $C_{L_{max}}$ with k tends to be quadratic. Nevertheless as the angular amplitude increases, the variation of the $C_{L_{max}}$ with k remains close to linear. This can be attributed to the effects of added mass mechanism which becomes more significant at higher reduced frequency.

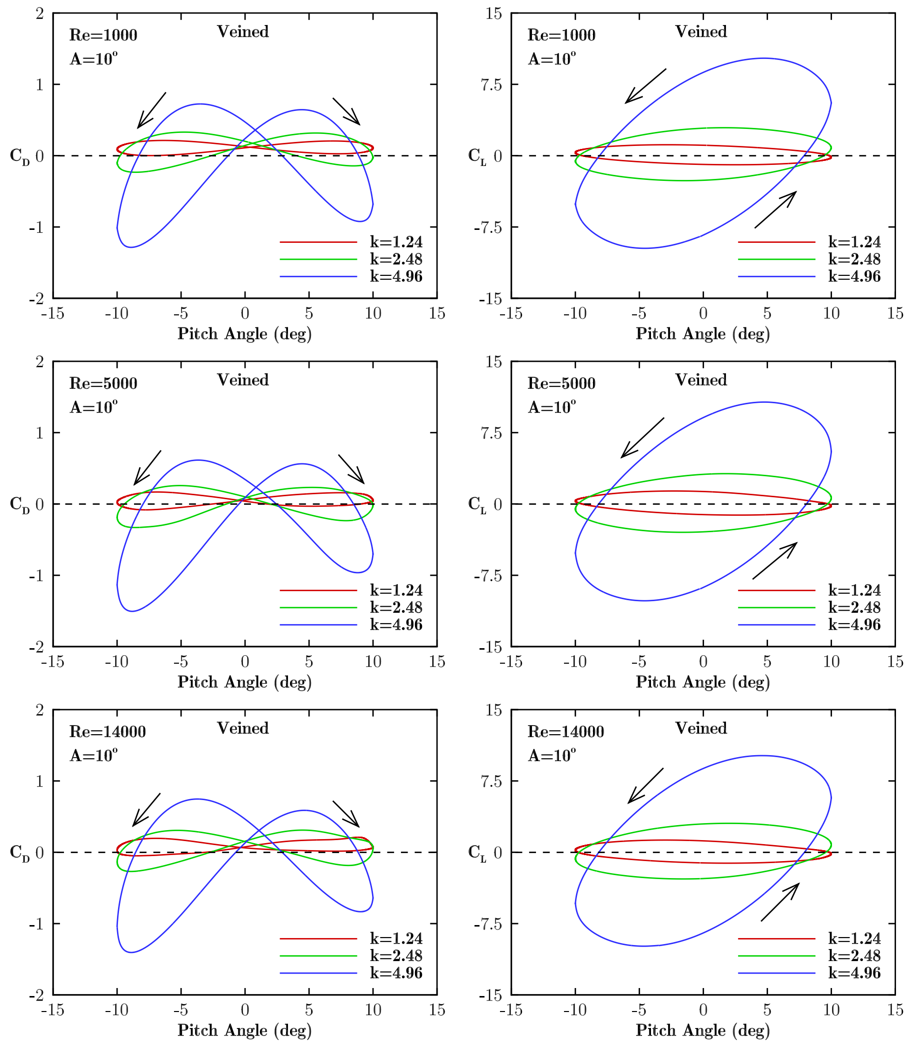

Figure 16: Lift and Drag coefficients of veined bio-airfoil calculated at A=10°, and different Reynolds numbers and reduced frequencies

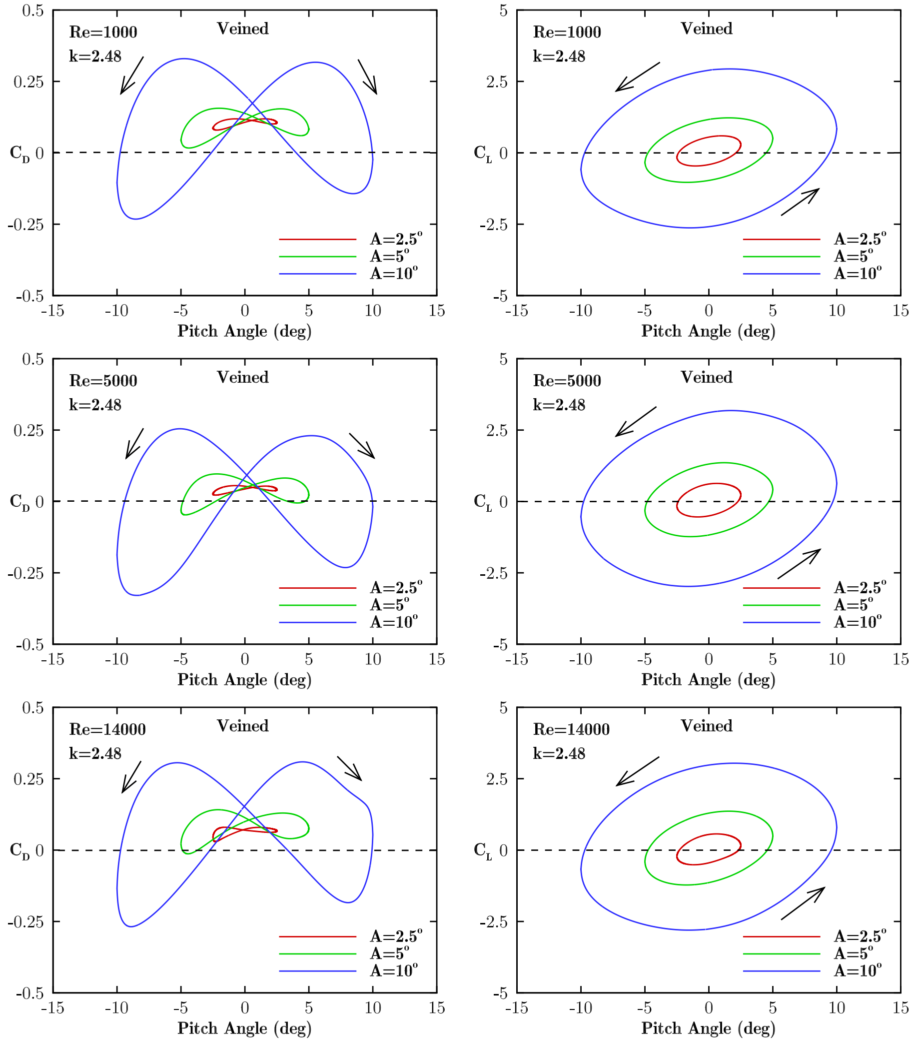

Figure 17: Lift and Drag coefficients of veined bio-airfoil calculated at k=2.48, and different Reynolds numbers and angular amplitudes

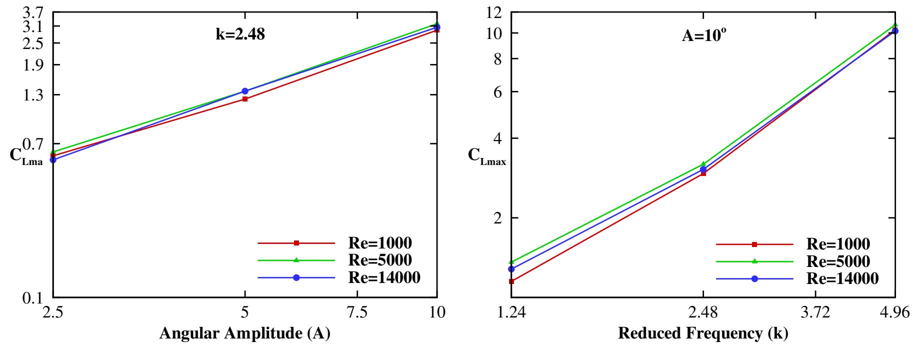

Figure 18: Lift and Drag coefficients of veined bio-airfoil calculated at A=10°, k=4.96 and different Reynolds numbers

Figure 19 shows the effect of Reynolds numbers on the dynamic hysteresis in lift and drag coefficients of veined bio-airfoil estimated at A=10°, k=4.96. Lift Coefficient of veined bio-airfoil are approximately the same at all Reynolds numbers. In laminar flow, increasing Reynolds number results decrement in C_D. The Drag coefficient of the bio-airfoils increased by moving from laminar to turbulent flow.

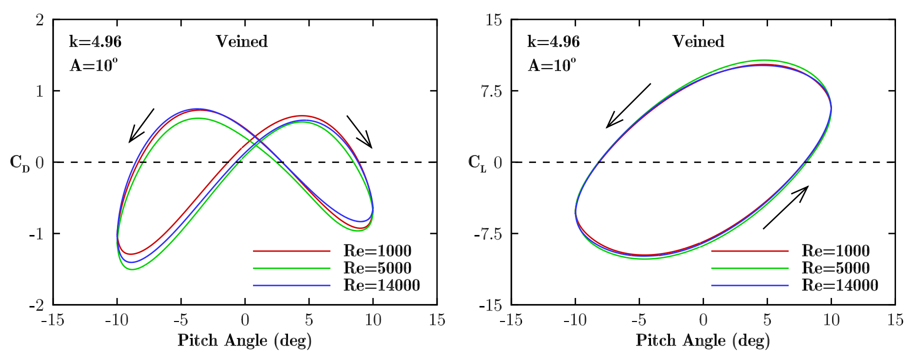

Figure 19: Lift and Drag coefficients of veined bio-airfoil calculated at A=10°, k=4.96 and different Reynolds numbers

5. SUMMARY AND CONCLUSIONS

In the framework of numerical simulation of air flow around a pitching corrugated bio-airfoil, it is required to study the effects of longitudinal veins topology on the aerodynamic characteristics of pitching bio-airfoils. In present study, the influence of cross sectional veins topology on the flow pattern and resulted aerodynamic performance of an oscillating corrugated bio-inspired airfoil was investigated. For this reason, the middle cross section of Ashena Cyanea wing was modeled with three configurations. The air flow passing bio-airfoil was subjected to three Reynolds numbers of 1000, 5000, and 14000 and selected reduced frequencies (k) and angular amplitude (A). The lift coefficients of the three studied bio-airfoils, over the range of Reynolds numbers, are close to each other considered in this work. At the Reynolds numbers of 1000 and 5000, the thin bio-airfoil has minimum drag coefficient and the drag coefficients of thick and veined bio-airfoils are quite similar. The veins in the bio-airfoils increase the drag coefficient significantly for the Reynolds numbers of 14000 compared to the Reynolds number of 5000. The hysteresis of lift and drag coefficients were provided through an increment for Reynolds number, reduced frequency, and angular amplitude.

Appendix A. Grid Convergence Index

Grid convergence index (GCI), as suggested by Roache [35], provides an error band for the CFD simulations and it can be an indicator to justify the resolution of the grid in a particular problem. The GCI for the grids defined as:

$$GCI_{mn} = \frac{F_s|\epsilon_{mn}|}{{r_{mn}}^p - 1} \ , \tag{A.1}$$

where F_s is a factor of safety. The factor of safety is considered to be $F_s = 3$ for comparisons of two grids and $F_s = 1.25$ for comparisons over three or more grids. Index n and m is level of the grid, which 1, 2, and 3 shows the fine, medium, and coarse grid, respectively. The relative error (ϵ) and the grid refinement ratio (r)

is defined as:

$$\epsilon_{mn} = \frac{f_n - f_m}{f_m} \tag{A.2}$$

$$r_{mn} = (\frac{N_m}{N_n})^{\frac{1}{D}} \tag{A.3}$$

where f is the CFD solution parameter, N is number of the grid cells, and D is dimension of the problem.

The order of grid convergence (p) involves the behavior of the solution error defined as the difference between the discrete solution ($f(h)$), and the exact solution (f_{exact}):

$$E = f(h) - f_{exact} = Ch^p + H.O.T \tag{A.4}$$

where C is a constant, p is the order of convergence, h is some measure of grid spacing, and $H.O.T$ is higher-order terms.

If the refinement ratio between the fine and medium grid (r_{12}) is not equal to that between medium and coarse grid (r_{23}), p is defined as [35]:

$$({r_{12}}^p - 1)({r_{23}}^p - 1)\varepsilon_{12} + ({r_{23}}^p - 1)\varepsilon_{12} - ({r_{12}}^p - 1)\varepsilon_{23} = 0 \tag{A.5}$$

where ε_{mn} defined as:

$$\varepsilon_{mn} = f_m - f_n \tag{A.6}$$

The Richardson extrapolation can be used to calculate the exact solution:

$$f_{exact} \approx f_1 + \frac{f_1 - f_2}{{r_{12}}^p - 1} \tag{A.7}$$

The maximum lift coefficient (Cl_{max}) within a cycle has been used to study the convergence of the simulations on different grids. The convergence study has been carried out for the veined bio-airfoil. The values of the Cl_{max} for fine ($350k$ cells), medium ($230k$ cells) and coarse grids ($115k$ cells) are 10.11, 10.17, and 10.29, respectively. In this regard, $p = 0.677$, $\epsilon_{12} = 0.006$, $\epsilon_{23} = 0.012$, $r_{12} = 1.233$, $r_{23} = 1.414$, $GCI_{12} = 4.93\%$, $GCI_{23} = 5.68\%$, and $Cl_{max_{exact}} = 9.72$.

References

[1] S. P. Sane, The aerodynamics of insect flight, Journal of experimental biology 206 (23) (2003) 4191–4208.

[2] W. Shyy, Y. Lian, J. Tang, H. Liu, P. Trizila, B. Stanford, L. Bernal, C. Cesnik, P. Friedmann, P. Ifju, Computational aerodynamics of low reynolds number plunging, pitching and flexible wings for mav applications, Acta Mechanica Sinica 24 (4) (2008) 351–373.

[3] R. Srygley, A. Thomas, Unconventional lift-generating mechanisms in free-flying butterflies, Nature 420 (6916) (2002) 660.

[4] C. P. Ellington, C. Van Den Berg, A. P. Willmott, A. L. Thomas, Leading-edge vortices in insect flight, Nature 384 (6610) (1996) 626–630.

[5] C. Lan, The unsteady quasi-vortex-lattice method with applications to animal propulsion, Journal of Fluid Mechanics 93 (04) (1979) 747–765.

[6] A. Azuma, S. Azuma, I. Watanabe, T. Furuta, Flight mechanics of a dragonfly, Journal of experimental biology 116 (1) (1985) 79–107.

[7] A. Azuma, T. Watanabe, Flight performance of a dragonfly, Journal of Experimental Biology 137 (1) (1988) 221–252.

[8] W. D. Savage SB, Newman BG, The role of vortices and unsteady effects during the hovering flight of dragonflies, Journal of Experimental Biology 83 (1) (1979) 59–77.

[9] A. L. Thomas, G. K. Taylor, R. B. Srygley, R. L. Nudds, R. J. Bomphrey, Dragonfly flight: free-flight and tethered flow visualizations reveal a diverse array of unsteady lift-generating mechanisms, controlled primarily via angle of attack, Journal of Experimental Biology 207 (24) (2004) 4299–4323.

[10] C. Hefler, R. Noda, H. Qiu, W. Shyy, Aerodynamic performance of a free-flying dragonfly—a span-resolved investigation, Physics of Fluids 32 (4) (2020) 041903.

[11] G. Rüppell, Kinematic analysis of symmetrical flight manoeuvres of odonata, Journal of Experimental Biology 144 (1) (1989) 13–42.

[12] S. Sudo, K. Tsuyuki, J. Tani, Wing morphology of some insects, JSME International Journal Series C Mechanical Systems, Machine Elements and Manufacturing 43 (4) (2000) 895–900.

[13] T. Flint, M. Jermy, T. New, W. Ho, Computational study of a pitching bio-inspired corrugated airfoil, International Journal of Heat and Fluid Flow 65 (2017) 328–341.

[14] C. J. Barnes, M. R. Visbal, Numerical exploration of the origin of aerodynamic enhancements in [low-reynolds number] corrugated airfoils, Physics of Fluids 25 (11) (2013) 115106.

[15] D.-E. Levy, A. Seifert, Simplified dragonfly airfoil aerodynamics at reynolds numbers below 8000, Physics of Fluids 21 (7) (2009) 071901.

[16] A. Vargas, R. Mittal, Aerodynamic performance of biological airfoils, in: 2nd AIAA Flow Control conference, Portland, OR, AIAA Paper, Vol. 2319, 2004.

[17] M. Tamai, Z. Wang, G. Rajagopalan, H. Hu, G. He, Aerodynamic performance of a corrugated dragonfly airfoil compared with smooth airfoils at low reynolds numbers, in: 45th AIAA Aerospace Sciences Meeting and Exhibit, 2007, pp. 1–12.

[18] X. G. Meng, M. Sun, Aerodynamic effects of wing corrugation at gliding flight at low reynolds numbers, Physics of Fluids 25 (7) (2013) 071905.

[19] M. Kwok, R. Mittal, Experimental investigation of the aerodynamics of a modeled dragonfly wing section, in: AIAA region I-MA Student Conference, Charlottesville, Virginia April, 2005, pp. 8–9.

[20] W.-K. Kim, J. H. Ko, H. C. Park, D. Byun, Effects of corrugation of the dragonfly wing on gliding performance, Journal of theoretical biology 260 (4) (2009) 523–530.

[21] K. Y. Okamoto Masato, A. Azuma, Aerodynamic characteristics of the wings and body of a dragonfly, Journal of Experimental Biology 199 (2) (1996) 281–294.

[22] A. B. Kesel, Aerodynamic characteristics of dragonfly wing sections compared with technical aerofoils, Journal of Experimental Biology 203 (20) (2000) 3125–3135.

[23] J. T. Murphy, H. Hu, An experimental study of a bio-inspired corrugated airfoil for micro air vehicle applications, Experiments in fluids 49 (2) (2010) 531–546.

[24] T. New, Y. Chan, G. Koh, M. Hoang, S. Shi, Effects of corrugated aerofoil surface features on flow-separation control, AIAA journal 52 (1) (2013) 206–211.

[25] A. B. Kesel, U. Philippi, W. Nachtigall, Biomechanical aspects of the insect wing: an analysis using the finite element method, Computers in biology and medicine 28 (4) (1998) 423–437.

[26] C. J. Rees, Form and function in corrugated insect wings, Nature 256 (5514) (1975) 200.

[27] K. Hord, Y. Liang, Numerical investigation of the aerodynamic and structural characteristics of a corrugated airfoil, Journal of Aircraft 49 (3) (2012) 749–757.

[28] R. Harbig, J. Sheridan, M. Thompson, Relationship between aerodynamic forces, flow structures and wing camber for rotating insect wing planforms, Journal of Fluid Mechanics 730 (2013) 52–75.

[29] R. Harbig, J. Sheridan, M. Thompson, Reynolds number and aspect ratio effects on the leading-edge vortex for rotating insect wing planforms, Journal of Fluid Mechanics 717 (2013) 166–192.

[30] L. T. K. Au, H. V. Phan, S. H. Park, H. C. Park, Effect of corrugation on the aerodynamic performance of three-dimensional flapping wings, Aerospace Science and Technology 105 (2020) 106041.

[31] G. N. Barakos, D. Drikakis, Unsteady separated flows over manoeuvring lifting surfaces, Philosophical Transactions of the Royal Society of London. Series A: Mathematical, Physical and Engineering Sciences 358 (1777) (2000) 3279–3291.

[32] G. Barakos, D. Drikakis, Computational study of unsteady turbulent flows around oscillating and ramping aerofoils, International journal for numerical methods in fluids 42 (2) (2003) 163–186.

[33] F. Menter, Y. Egorov, The scale-adaptive simulation method for unsteady turbulent flow predictions. part 1: theory and model description, Flow, Turbulence and Combustion 85 (1) (2010) 113–138.

[34] F. R. Menter, Best practice: scale-resolving simulations in ansys cfd, ANSYS Germany GmbH 1.

[35] P. Roache, Perspective - a method for uniform reporting of grid refinement studies, Journal of Fluids Engineering-Transactions of the ASME 116 (3) (1994) 405–413. doi:10.1115/1.2910291.

[36] P. Sooraj, A. Sharma, A. Agrawal, Dynamics of co-rotating vortices in a flow around a bio-inspired corrugated airfoil, International Journal of Heat and Fluid Flow 84 (2020) 108603.

[37] J.-Y. Andro, L. Jacquin, Frequency effects on the aerodynamic mechanisms of a heaving airfoil in a forward flight configuration, Aerospace Science and Technology 13 (1) (2009) 71–80.